

# Discovery of an Extreme Quasar-mode Feedback on 100 kpc Scale at $z=2.3$ in an Enormous Ly $\alpha$ Nebula

## Abstract

Feedback now appears as an attractive mechanism to resolve some of the outstanding problems with the modern cosmological model. Evidences of radiation-pressure driven feedbacks on 100 kpc have been reported in "Quasars Probing Quasars" survey through absorptions while they are not probed by the emission observations. Here we report the Keck Cosmic web Imager (KCWI) spectroscopic observations targeting on an enormous Ly $\alpha$  nebula known as MAMMOTH-1 in the density peak of BOSS1441 protocluster at  $z \approx 2.3$ . We confirm that this enormous Ly $\alpha$  nebula is powered by a radio-quiet, complex interacting galaxy system. Reaching a surface brightness of  $6.4 \times 10^{-18} \text{ erg s}^{-1} \text{ cm}^2 \text{ arcsec}^{-2}$ , our observations clearly reveal 88 kpc CIV emission and 80 kpc He II emission. The follow-up near-infrared observations further reveal the H $\alpha$  emission on 122 kpc scale. Besides, all of Ly $\alpha$ , HeII and CIV emissions have a double-peak structure throughout the nebula and the flux-weighted velocity maps constructed from the three emissions show the clear velocity gradients along the same direction with the velocity offset of  $\Delta v = 1000 \text{ km/s}$  and FWHM of  $\sigma_v > 1400 \text{ km/s}$ . With these evidences, we confirm there is an extremely powerful outflow from the galaxy system. The outflow energy rate reaches to  $\dot{E}_{\text{out}} \approx 3 \times 10^{45} \text{ erg/s}$  which is probably the highest comparing to previous observations. By comparing our results with simulations, we find only quasar-mode feedback can naturally explain these observations. This new discovery of such an extreme quasar-mode feedback on 100 kpc scales at  $z > 2$  will put constraint on the cosmological simulations and help us to further understand the role of feedback in the coevolution of galaxies and their environments.

*Key words:* Galaxies – Enormous Ly $\alpha$  Nebula – AGN feedback – outflow

## 1. Introduction

Over the past few decades it has been realized that the black hole (BH) at the centre of a galaxy bulge is more than just decorations but plays a key role in galaxy evolution (Fabian 2012). This process is known as Active Galactic Nucleus (AGN) feedback which takes place by accreting matter onto the massive BH and have a profound effect on galaxy evolution even the large-scale structure comparing with the large ratio of the size of BH to host galaxy. For example, the energy released to build a BH with mass  $M_{\text{BH}} = 10^8 M_{\odot}$  would correspond to  $E_{\text{BH}} \approx 0.1 M_{\text{BH}} c^2$ . This total accretion energy is two-to-three orders of magnitude higher than the binding energy of the galaxy bulge the BH resides in, and is comparable to, even higher than, the thermal energy of the gas in the dark matter halo (Harrison 2016). So feedback induced by massive BH is able to change the evolution path of galaxies and observations are required to constrain details of this process.

After decades of studies, two sorts of AGN feedback models have been developed. The first one is the radio mode feedback also known as maintenance mode or kinetic mode, it is believed that this mode is the most efficient mechanism in low redshift clusters, at late times and during periods of low

BH accretion rates. The objects that are responsible for this type of feedback are likely to be low-excitation radio AGN which has low accretion rate and are always companied by radio lobes (Churazov et al. 2005; Bower et al. 2006; McCarthy et al. 2011). This feedback model can naturally solves the "cut-off" of the galaxy luminosity function, cooling flow problem and so on (Bower et al. 2006; Croton et al. 2006; Somerville et al. 2008). In addition, another powerful mode of feedback happens during periods of rapid accretion known as quasar mode or radiative mode. AGN with high accretion rate is responsible for this type of feedback. This mode basically requires 0.005-0.15 of the accretion energy to couple to the cold gas within the host galaxy and to expel this gas through outflows. This ultimately results in the shut-down of future BH growth or star formation (Benson et al. 2003; Hopkins & Beacom 2006; DeBuhr et al. 2012). Nevertheless, it has been also prompted that, this mode of feedback could induce positive feedback which trigger star formation by inducing pressure in cold gas reservoirs (Nayakshin & Zubovas 2012; Ishibashi & Fabian 2012; Silk 2013). Analytical models have already used it to explain  $M_{\text{BH}} - M_{\text{bulge}}$  relationship (Fabian 1999; Granato et al. 2004; King et al. 2011; Faucher-Giguère & Quataert 2012) and this mode is also required to explain the chemical enrichment of intercluster medium (ICM) and circumgalactic medium CGM) (Bor-

gani et al. 2008; Wiersma et al. 2009; Fabjan et al. 2010; Ciotti et al. 2010).

Spectroscopy is used as a direct way to search for outflows. Such observations have identified outflows in ionized, atomic and molecular gas (Nesvadba et al. 2008). The high-velocity [OIII] $\lambda$ 5007 emission line is widely used to search for outflowing ionized gas. These studies have used only one-dimensional spectra and therefore provide no insight on the spatial extent or structure of the outflow. Nevertheless, the spatial information is crucial to study the outflow, such as the three-dimensional kinematics. This information help us to further understand how feedback influences the coevolution of the host galaxies with the gas environment and also provide us information about the metallicity of CGM and ICM. Harrison et al. (2014) used integral field unit (IFU) observations covering [OIII] $\lambda$ 4959, 5007 and  $H\beta$  emission lines to study the outflows of 16 type-2 AGN at  $z < 0.2$ . They found high-velocity ionized gas with observed spatial extents of 6-16 kpc. Their study demonstrates that galaxy-wide energetic outflows are not confined to the most extreme star-forming galaxies or radio-luminous AGN. In another observations, Rupke et al. (2019) show optical integral field observations of the low-redshift galaxy SDSS J211824.06+001729.4 with Keck Cosmic Web Imager (KCWI), the OII $\lambda$ 3726, 3729 emission lines reveal an ionized outflow powered by starburst spanning 80 by 100 square kpc.

At the redshift of  $z = 1 - 3$ , the peak period of cosmic star formation, the jets have even been discovered on scale of 100 kpc by observing either the radio lobes or x-ray cavities. Meanwhile, some studies also suggest quasars have the ability to ionize and accelerate dense clumps of material on sub-kpc scales while quasar feedbacks are even invoked on larger scales. Previous "Quasars Probing Quasars" (QPQ) survey have found signatures of quasar-mode feedback in the cool CGM through absorptions studies (Prochaska et al. 2013; Hennawi & Prochaska 2013; Lau et al. 2016). For example, Lau et al. (2016) used CIV absorptions to trace the velocity field in CGM. They found, on 100 kpc, the velocity dispersion of CIV can still reaches to  $\sim 500$  km/s which may indicate intense activities. These results suggest quasar-mode feedback has the ability to significantly affect the CGM of quasars. In theoretical aspect, many works use the approach of hydrodynamical numerical simulation to study the AGN feedback in galaxy formation and evolution (Springel et al. 2005; Di Matteo et al. 2005; Ciotti & Ostriker 2007; Sijacki et al. 2007; Booth & Schaye 2009; Ostriker et al. 2010; Hirschmann et al. 2014; Ciotti et al. 2017). Although some simulations (Faucher-Giguère et al. 2016) are able to reproduce the high covering fraction of optically thick gas, their velocity fields are not extreme enough.

Nevertheless, the QPQ survey and other absorption-line studies are limited by the relatively small sample size of bright, background sources which is hardly to provide more than one sightline passing through any halo. To resolve the spatial distribution, global kinematics and key properties of the gas, emission studies of medium are needed. Owing to its diffuse nature, such observations are generally extremely dif-

ficult, but the newly on-board KCWI, an integral field spectroscopy are able to push surface brightness limits down to a few  $\times 10^{-19}$  erg s $^{-1}$  cm $^2$  arcsec $^{-2}$  and better. This make it possible to directly probe the metal-enriched CGM through emission. In this premise, we report the follow-up observations of Cai et al. (2017b) on the ELAN with KCWI. This is a newly-onboard integral field spectrograph equipped on Keck Telescope which provides us the ability to capture the very weak photons from the gas in cosmic web. As a result, by using KCWI we reach a deep surface brightness of  $2.2 \times 10^{-18}$  erg s $^{-1}$  cm $^2$  arcsec $^{-2}$  and completely reveal the three-dimensional kinematics of Ly $\alpha$  on the scale of 175 kpc (limited by instrument FoV) which is the full KCWI field of view. Other than Ly $\alpha$ , the data also presents extended HeII and CIV emission up to 90 kpc. The three-dimensional kinematics extracted from these emissions further confirm the extreme quasar-mode feedback powered by BOSS1441. The paper is structured as follows, in §2 we give details of IFU observations and data preprocessing. In §3 we present the optimal-extracted images and moment maps of these emission lines. Models used to estimate outflow energy are also presented in this section. In §4 we discuss the possible mechanisms powering Ly $\alpha$  nebula the outflow. Finally we give a brief summary in §5. Throughout this paper, we assume a flat cosmological model with  $\Omega_\Lambda = 0.7$ ,  $\Omega_M = 0.3$  and  $H_0 = 70$  km s $^{-1}$  Mpc $^{-1}$ . In this cosmology,  $1'' \approx 8.2$  kpc at  $z = 2.3$ .

## 2. Observations

### 2.1. KCWI Instrument Configuration

In this section, we provide details on the observations and KCWI instrument configurations. We obtained IFU spectroscopy of BOSS1441 on UT-20180518 with KCWI on Keck-II. The large slicer, with Field of View (FoV) of  $20'' \times 33''$ , was employed for these observations which has the spatial resolution of  $\approx 1.35''$ . We choose this slicer because it possesses the largest FoV to cover MAMMOTH-1. We also employed blue BL1 grating centered at  $\lambda = 4500$  Å which gives a usable wavelength coverage of 3500 – 5600 Å. This is an excellent regime to perform studies of Ly $\alpha$  nebula at  $z \approx 2.3$ . This configuration yields a slit-limited spectral resolution of  $R \approx 1000$  (rest-frame 300 km/s) which is high enough to fully resolve the kinematics of MAMMOTH-1. The total on-source exposure time is 4 hours conducted with two pointings, we integrated for 2 hours consisting of 6 exposures of 20 min for each pointing. This exposure time allows us to reach a surface brightness equals to  $7 \times 10^{-19}$  erg s $^{-1}$  cm $^2$  arcsec $^{-2}$ . We didn't apply nod-and-shuffle, instead we interleaved observations for a nearby patch of sky ( $\Delta RA = +2'$ ,  $\Delta DEC = +1'$ ) for 4 hours to later perform sky subtraction, a standard star was also observed for flux calibration purposes.

### 2.2. HST Broadband Imaging

The broadband image was obtained with Hubble Space Telescope (HST) Wide Field Camera 3 (WFC3) in the F160W filter (ID: 14760; PI: Z. Cai). For MAMMOTH-1

at  $z = 2.31$ , the infrared F160W filter covers the rest-frame wavelength range of 4200-5100 Å. The observations were performed on 2017 September 07 with the exposure time of 2212 seconds. The data were then calibrated by the data processing software system version COMMON 2017\_2a.

### 2.3. Data Reduction

The data was reduced using the XXX pipeline. In this process, we first subtracted bias, corrected the variation by dividing the flat-field images from each raw image, removed cosmic-rays and created error images. Then we did geometric transformation and wavelength calibration. Finally we calibrated flux for each image with the spectrophotometric standard star. With all of these done,  $\sigma$  clipping was performed for each sky cube by masking pixels with value  $3\sigma$  above the median, then we used the masked cube to estimate the sky channel-by-channel and subtracted it from the reduced data cube.

### 2.4. 3D mask construction

The final step is to construct the three-dimensional segmentation mask (3D mask) in order to obtain the low-dimensional projections of the extracted sources, such as optimally-extracted images and flux-weighted-moment maps, for further analysis. We produce the 3D mask based on the user-defined signal-to-noise ratio (SNR) threshold, pixels in data cube with value lower than the threshold are masked which means the value of the corresponding pixels in 3D mask is 0, otherwise 1. Because this process is based on the SNR threshold, the estimation of the background noise is essential. This noise is estimated under the assumption that background noise of each wavelength layer in the data cube shares the same value. This assumption allows us to calculate the standard deviation with parts of the data cube which do not contain either the emission nor the absorption components and apply it to the whole data cube. The SNR threshold is set to be  $2\sigma$  which typically corresponds to a flux density of  $10^{-18} \text{ erg s}^{-1} \text{ cm}^{-2} \text{ Å}^{-1}$ .

After this preliminary work, we find widely extended HeII and CIV emission and an extremely powerful outflow on 100 kpc which is rarely seen before at high redshift. In §3 we show our results to confirm this outflow and in §4 we give detailed discussion.

## 3. Results

### 3.1. Radio Emission

Emonts et al. (2019) used sensitive low-surface-brightness observations of Very Large Array (VLA) to trace the cold molecular gas in the inner region of MAMMOTH-1 by detecting the CO (1-0) emission. They found four CO sources which are a few kpc away from the associated galaxies or groups. This result suggests that the core of the potential well of this Ly $\alpha$  nebula is marked by the cold gas rather than the obscured AGN. Since none of the continuum image (center on 35 GHz and 150 GHz) from VLA nor Atacama Large Millimeter/submillimeter Array (ALMA) shows detectable signal, we use them to give a  $3\text{-}\sigma$  upper limit on its continuum

emission in radio band,  $f_{35, \text{up}} = 0.050 \text{ mJy}$ ,  $f_{150, \text{up}} = 0.066 \text{ mJy}$ . By applying these two upper limits with the data from Arrigoni Battaia et al. (2018a), we fit the spectral energy distribution (SED) of BOSS1441 with M82 template from Silva et al. (1998) in Fig. 1. Gray lines represent the SED of radio-quiet galaxies in Harrison et al. (2014) with the gray square representing the flux density at 1.4 GHz (rest frame) of these sources. The purple points represent the flux of MRC 1138-262 which is also known as spiderweb galaxy with extreme radio emission at  $z=2.16$  (Nesvadba et al. 2006). The brown dashed line is the average of SEDs belonging to 1056 radio galaxies (RG) with redshifts in the range of 0.0028 – 1.7 (Toba et al. 2019). All of these SEDs and data have been normalized and shifted to  $z = 2.31$ . M82 template fits extremely well with flux of source-B even including the two upper limits from ALMA and VLA, this evidence suggests that source-B should be a star burst galaxy. In addition, the departure of flux of source-B and M82 template from RG template and flux of spiderweb galaxy indicates that there should be no strong radio emission from source-B due to AGN activity.

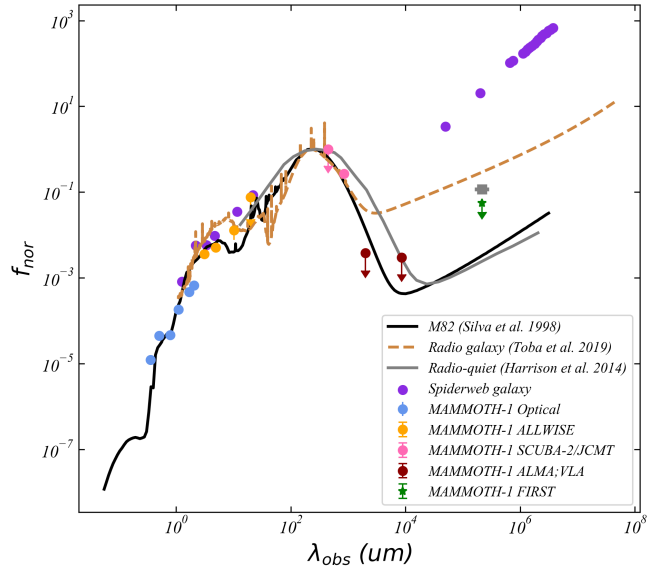


**Figure 1:** SED for source-B powering ELAN MAMMOTH-1. The data points are from Cai et al. (2017b) (blue), ALLWISE source catalog, SCUBA-2 data (Arrigoni Battaia et al. 2018a) (magenta), ALMA and VLA continuum images (Emonts et al. 2019) (dark red) and FIRST catalog (green). Gray line represents SED of radio-quiet galaxy while gray square represents flux at 1.4 GHz of "radio-excess" galaxy Harrison et al. (2014). The brown dashed line is the average template of 1056 radio galaxies at redshifts from 0.0028 to 1.7 (Toba et al. 2019). All of this data are normalized and shifted to  $z=2.3$ .

We calculate the ratio ( $q_{\text{IR}}$ ) between the far-infrared flux (8 – 1000  $\mu\text{m}$ ) and radio flux with the definition given by Ivison et al. (2010). This ratio is usually used to identify if there is significant radio emission above that expected from their star-formation activity (radio emission results from AGN or

other process). The formula is given by:

$$q_{\text{IR}} = \log\left[\frac{S_{\text{IR}}/3.75 \times 10^{12} \text{ W m}^{-2}}{S_{1.4}/\text{W m}^{-2} \text{ Hz}^{-1}}\right] \quad (1)$$

where  $S_{\text{IR}}$  is the rest-frame flux in far-infrared range (8 – 1000  $\mu\text{m}$ ) and  $S_{1.4}$  is the flux density at 1.4 GHz in rest frame. The far-infrared luminosity is  $L_{\text{IR}} = 3.2 \times 10^{12} L_{\odot}$  estimated by Arrigoni Battaia *et al.* (2018a). Through setting the luminosity distance to be  $D_L = 18773.8$  Mpc at redshift  $z=2.3$ , it is easy to calculate the far-infrared flux  $S_{\text{IR}} = 2.9 \times 10^{-16} \text{ W cm}^{-2}$ . Because the D-configuration of VLA doesn't cover  $\nu_{\text{obs}} = 0.42$  GHz (1.4 GHz in rest frame), we adopt  $S_{1.4}=0.01$  mJy from M82 SED template. We note here that the constrain of continuum,  $f_{150,\text{up}}$ , is one-order-magnitude lower than that of M82 SED template, therefore the true flux density at  $\nu_{\text{rest}} = 1.4$  GHz is possibly lower than 0.01 mJy. By adopting  $S_{1.4} = 0.01$  mJy the low limit of  $q_{\text{IR}}$  is equal to 1.9. Ivison *et al.* (2010) and Del Moro *et al.* (2013) define "radio-excess" sources as those with  $q_{\text{IR}} \leq 1.8$ , this calculation also supports that source-B has no significant radio emission.

Based on these evidences we conclude that source-B is most likely a radio-quiet quasar with no strong radio emission due to AGN activity.

### 3.2. Morphology and Emission

We construct continuum-free line images by summing over the wavelength range of the emission lines in data cubes and subtracting the underlying continuum component from them. The continuum component is estimated by taking average from another wavelength range without emission nor absorption. We show the results in the left panel of Fig. ?? . The three contours of different colors representing different emissions show the spatially extended emission of Ly $\alpha$  HeII and CIV with the first contour corresponding to  $2\sigma$  and steps between contours to  $2\sigma$ . The background image was taken by Wide Field Camera 3 (WFC3) on Hubble Space Telescope (HST) with F160W filter. Sources labeled from G-1 to G-5 are galaxies at the same redshift ( $z \approx 2.3$ ) with Source-B confirmed by CO (1-0) emission and CO (3-2) emission (Emonts *et al.* 2019; Li *et al.* 2020). The emitting structure shows Ly $\alpha$  nebula covers all of the marked objects and extends to  $20''$  which corresponds to 164 kpc. It also shows that the physical projected size of extended HeII and CIV emission reaches to  $9''$  corresponding to 74 kpc.

Spectra are extracted within aperture with radius of  $1.5''$  centering on the peak of emission (larger than the spatial resolution of KCWI) and shown in the right panel. To determine the redshifts of these widely extended nebulae, we fit the three emission lines with one-component gaussian function and estimate the wavelength of line centre. The fitted parameters are shown in Tab.1. By converting the line width ( $\text{\AA}$ ) to FWHM (km/s) it seems that all of the three emission line have a relatively large FWHM which equals to  $\text{FWHM}_{\text{Ly}} = 1225$  km/s,  $\text{FWHM}_{\text{HeII}} = 1039$  km/s and  $\text{FWHM}_{\text{CIV}} = 1786$  km/s. This result indicates that there

may be extremely violent kinematic activity in the nebula on a physical scale of 100 kpc.

Because the surface brightness (SB) values for both kinematically narrow and broad features would have been either lost in the noise or underestimated in a narrow-band (NB) image with single width of wavelength, we adopt optimally-extract method from Borisova *et al.* (2016) to construct optimally-extracted images which can reach to a larger dynamic range comparing to a standard image. These images are obtained by using a three dimensional segmentation mask (3D mask) which defines a three-dimensional SNR surface in the cube, pixels with values below the SNR threshold are masked and only pixels possessing signal beyond threshold are extracted. Therefore, the signal of each pixel are integrated along a slightly different range in wavelength which allows us to obtain images or spectra with maximal SNR after stacking along spatial axis or spectral axis. In particular, images presented in Fig. ?? (left column) are obtained by using this method after continuum-subtraction and stacking along spectral axis. The three extended emissions are detected at faint levels with  $1-\sigma$  SB of  $\text{SB}_{\text{Ly}} = 6.4 \times 10^{-19} \text{ erg s}^{-1} \text{ cm}^2 \text{ arcsec}^{-2}$ ,  $\text{SB}_{\text{HeII}} = 9.2 \times 10^{-19} \text{ erg s}^{-1} \text{ cm}^2 \text{ arcsec}^{-2}$  and  $\text{SB}_{\text{CIV}} = 3.8 \times 10^{-18} \text{ erg s}^{-1} \text{ cm}^2 \text{ arcsec}^{-2}$ .

We also obtain the NB image of H $\alpha$  emission with MOIRCS on Subaru Telescope by using the BrG filter centering on  $2.165 \mu\text{m}$  shown in Fig. ?? (left panel). This result reveals the H $\alpha$  emission on  $14.5''$  which corresponds to 122 kpc primarily from south to north. The similarity between the shape of H $\alpha$  and Ly $\alpha$  may indicate they have the same powering mechanism. It has a typical surface brightness of  $\text{SB}_{\text{H}\alpha} = 1.2 \times 10^{-18} \text{ erg s}^{-1} \text{ cm}^2 \text{ arcsec}^{-2}$  and luminosity of  $L_{\text{H}\alpha} = 2.8 \times 10^{43} \text{ erg/s}$ . This extended H $\alpha$  emission beyond 100 kpc is also rarely seen at  $z \approx 2$ . Leibler *et al.* (2018) suggests the ratio between Ly $\alpha$  emission and H $\alpha$  emission can be used as an indicator of the powering mechanism of the nebula. And since Ly $\alpha$  and H $\alpha$  emission have a large overlap area, we then obtain the two-dimensional ratio map and present it in ?? (right panel). It reveals H $\alpha$  nebula is divided into two parts. The northwest part, "region 1", possesses large ratio but small size and the southwest part, "region 2", has small ratio but large size. "Region 1" shows the ratio decreases from the edge to center with mean value of 0.314 while "Region 2" has the mean value of 6.8. Since "region 1" is compact and overlays on G-1, it is probably emitted from the interstellar medium (ISM) of G-1 instead of the CGM.

	$\lambda_c(\text{\AA})$	$\sigma_\lambda(\text{\AA})$	$L(\text{erg/s})$	redshift
Ly $\alpha$	4024	7	$2.68 \times 10^{44}$	2.310
HeII	5438	8	$1.97 \times 10^{43}$	2.316
CIV	5143	13	$2.29 \times 10^{43}$	2.320

Table 1:



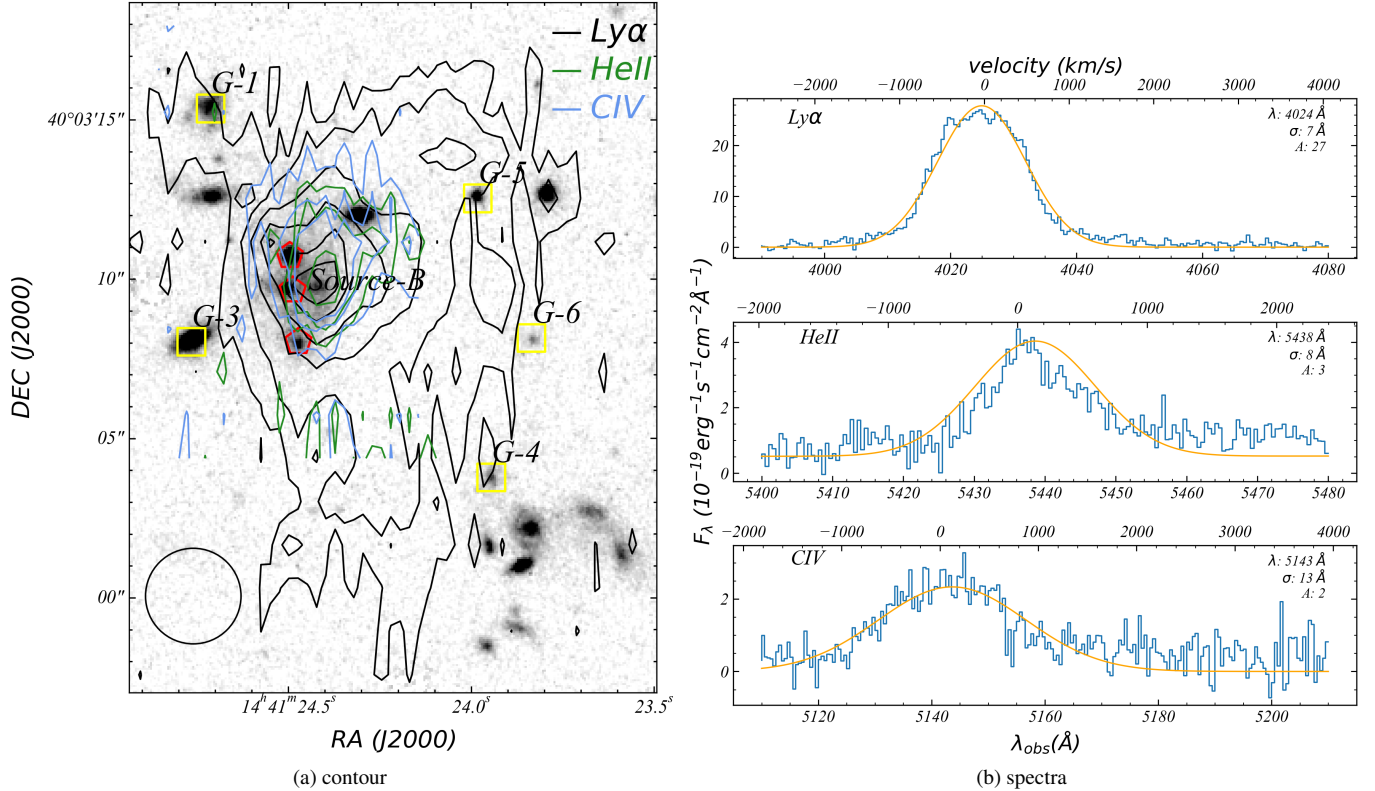


**Figure 2:** Left: HST BW image of MAMMOTH-1 from WFC3 PI: Cai. We overlay the contours of Ly $\alpha$ , HeII and CIV emissions on it. Black contours represent Ly $\alpha$ , blue contours represent HeII emission while green contours represent CIV emission. We mark source-B with red color and sources at the same redshift with yellow color. The spatial resolution of KCWI is shown in the left bottom. Right: spectra of the 3 emission lines extracted from aperture center on source-B with radius  $1''$ , we fit them with one-component gaussian function.

### 3.3. Three Dimensional Kinematics

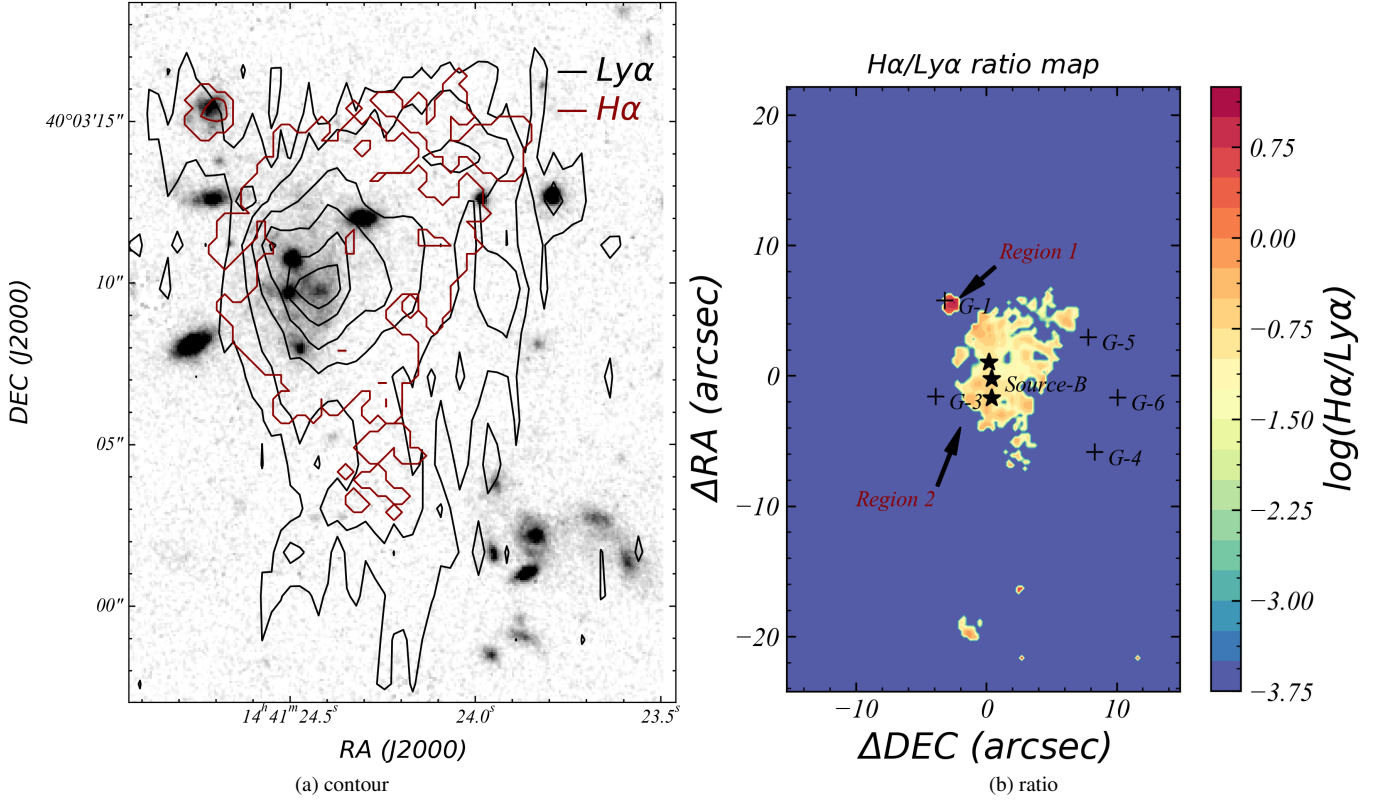
In this section we present the maps for flux-weighted velocity and flux-weighted dispersion of Ly $\alpha$ , HeII and CIV emissions produced with the 3D mask to get an indication of kinematic patterns. We note that Ly $\alpha$  resonant scattering effect doesn't play an important role on kinematics in the central area because it tends to disrupt the coherency of kinematics instead of enhancing it (Cantalupo et al. 2005), this is also confirmed by the results of HeII and CIV emissions.

Fig. ?? shows the moment maps together with the optimally-extracted images of the three emissions. The optimally-extracted images in left panel clearly shows the projected physical scale of Ly $\alpha$  emission extends to 175 kpc which approximates the typical size of dark matter halo at this redshift. This projected scale is smaller comparing to the results of Cai et al. (2017b) due to small FoV ( $20'' \times 33''$ ) of KCWI. In addition, HeII and CIV emission also extends to tens of kpcs surpassing the typical size of galaxies, especially CIV emission which extends to 88 kpc. This spatially very extended metal emissions are rarely seen at high redshift.

In the middle and right panel we present the maps of first and second moment of flux distribution. The middle panel represents the flux-weighted centroid velocity maps, it shows that there are evident velocity gradients in the three

velocity maps with same direction from the northwest to the southeast. This kinematic pattern is usually the indication of rotating gas disk in CGM or outflow ejected from central AGN. Besides, the velocity map of Ly $\alpha$  emission also shows gradient around G-5 from northeast to southwest. The velocity dispersion map of Ly $\alpha$  emission shows that the area around source-B possesses larger velocity dispersion ( $\sigma_v > 400 \text{ km/s}$ ) and extends to  $\sim 80 \text{ kpc}$ . In some spatial positions, dispersion is even larger than 650 km/s which corresponds to FWHM of 1550 km/s. Following the same method in Arrigoni Battaia et al. (2018) the expected velocity dispersion calculated for a dark matter halo hosting quasars is  $\sim 300 \text{ km/s}$  with the results  $M_{\text{DM}} \approx 10^{13} M_\odot$  in Cai et al. (2017b) where  $M_{\text{DM}}$  is the mass of dark matter halo. The significant comparison between expected dispersion and our results may indicate that there is extremely powerful kinematic activity in this region which is impossible caused by rotation or inflow.

Fig. ?? shows the channel map of Ly $\alpha$  emission with step of 200 km/s. It is clearly seen that the red component and blue component are on either side of source-B. Besides, We also extract the spectra from different spatial positions which are normalized and fitted with one-component gaussian function and show it in Fig. ?. We adopt circular aperture with



**Figure 3:** Left: HST image of MAMMOTH-1 from circle 24,25, PI: Cai. We overlay on it  $\text{Ly}\alpha$  HeII and CIV psudo narrow band images. Black contour is  $\text{Ly}\alpha$ , blue contour is HeII, green contour is CIV. We also mark source-B with red mark and sources at the same redshift with yellow mark. We also plot circle with raidus of  $1\text{arcsec}^2$ . Right: spectra of the 3 emission lines extracted from aperture center on source-B with radius  $1\text{arcsec}^2$ , we fit them with one-component gaussian function.

radius of  $1.5''$ . As a result, the movement of  $\text{Ly}\alpha$  is clearly seen.

Based on the above analysis, we rule out the possibility that the kinematic pattern is result from rotating gas disk, inflow and resonant scattering effect of  $\text{Ly}\alpha$  emission. Together with the existing of extended HeII, CIV and OIII emissions (Cai et al. 2017b), the most natural and straightforward interpretation is that there is extremely powerful and widely influenced outflow ejected from source-B which has the ability to influence the gas environment in dark matter halo hosting source-B. The effect of feedback on large scale has been widely reported before, however these outflows are usually powered by jet with significant radio signal. So, the halo-scale-influenced outflow with no strong radio signal at high redshift makes our observation unique. As a consequence, understanding the mechanism powering this strong outflow in our observation is essential for feedback effect on galaxy evolution.

### 3.4. Model of the outflow

The mass rate, energy rate and momentum rate being carried by outflow are important to help us understand the physical mechanisms driving the outflow. Although outflow are likely to be entraining gas in multiphases, the cool and warm

gas observed here could represent a large fraction of the overall mass and energy of the total outflows. Because of the complication of modeling outflows, here we adopt simple outflow models to provide first order constraints. Following the same process of Harrison et al. (2014), the outflow energy rate is estimated with two methods which give the upper limit and low limit respectively. We calculate the mean value of these limits in logarithmic space and use it as the fiducial value. The low limit is given by Eq.7 in Rodriguez Zaun et al. (2013):

$$\dot{M} = \frac{3L_{\text{Ly}\alpha} v_{\text{out}}}{\alpha_{\text{Ly}\alpha}^{\text{eff}} h\nu_{\text{Ly}\alpha} n_e r} \quad (2)$$

where  $L$  is the luminosity of  $\text{Ly}\alpha$  emission,  $m_p$  is the proton mass,  $v_{\text{out}}$  is outflow velocity,  $\alpha_{\text{Ly}\alpha}^{\text{eff}}$  is recombination coefficients which is obtained from Storey & Hummer (1995),  $h\nu_{\text{Ly}\alpha}$  is the energy of  $\text{Ly}\alpha$  photons,  $n_e$  is electron density and  $r$  is the radius of the outflow to its host, we adopt  $r = 30$  kpc for our case. The kinetic power of the outflow  $\dot{E}$  relating to the velocity dispersion, mass outflow rate and outflow velocity is also given by Rodriguez Zaun et al. (2013):

$$\dot{E} = \frac{\dot{M}}{2} (v_{\text{out}}^2 + 3\sigma^2) \quad (3)$$

the main uncertainty in calculating the mass outflow rates is electron density which is often measured from the emission-

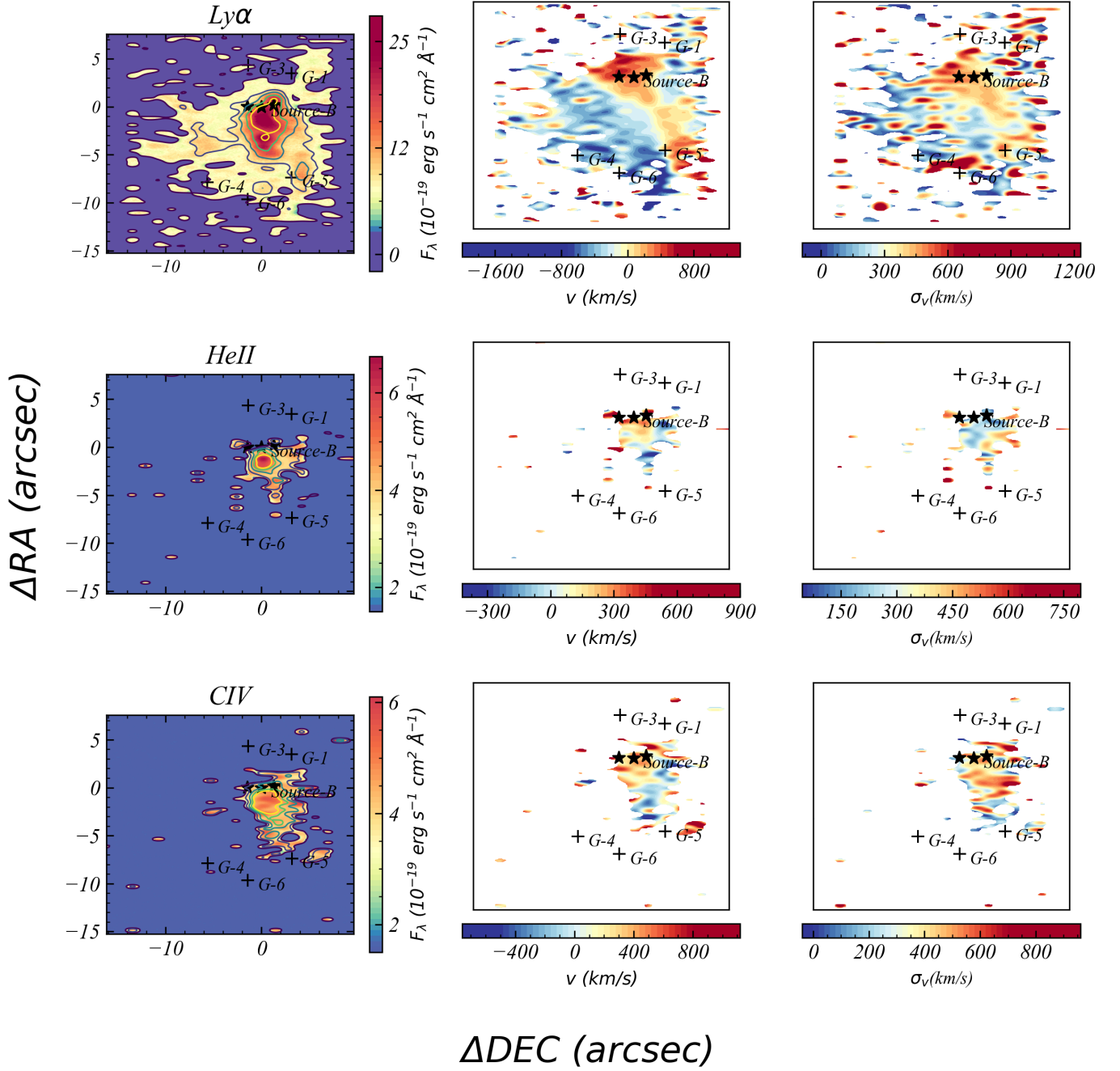


**Figure 4:** Left: continuum-subtracted optimally extracted images for the 3 emissions. These images are obtained by stacking each slice together. Pixels with value  $< 1.5\sigma$  are masked for each slice. The contour represent signal-to-noise ratio(SNR). We adopt  $(5\sigma, 9\sigma, 18\sigma, 30\sigma, 42\sigma, 51\sigma)$ ,  $(3\sigma, 5, 9\sigma)$  and  $(4\sigma, 7\sigma, 9\sigma)$  for Ly $\alpha$ , HeII and CIV respectively. Middle: flux-weighted velocity map obtained from the first-moment of flux distribution with respect to the systemic redshift of MAMMOTH-1. Right: flux-weighted velocity dispersion obtained from the second-moment of the flux distribution. Sources at the same redshift with MAMMOTH-1 confirmed by CO (2-1) emission (Emonts et al. 2019) and CO (3-2) emission (Li et al. 2020) are also marked.

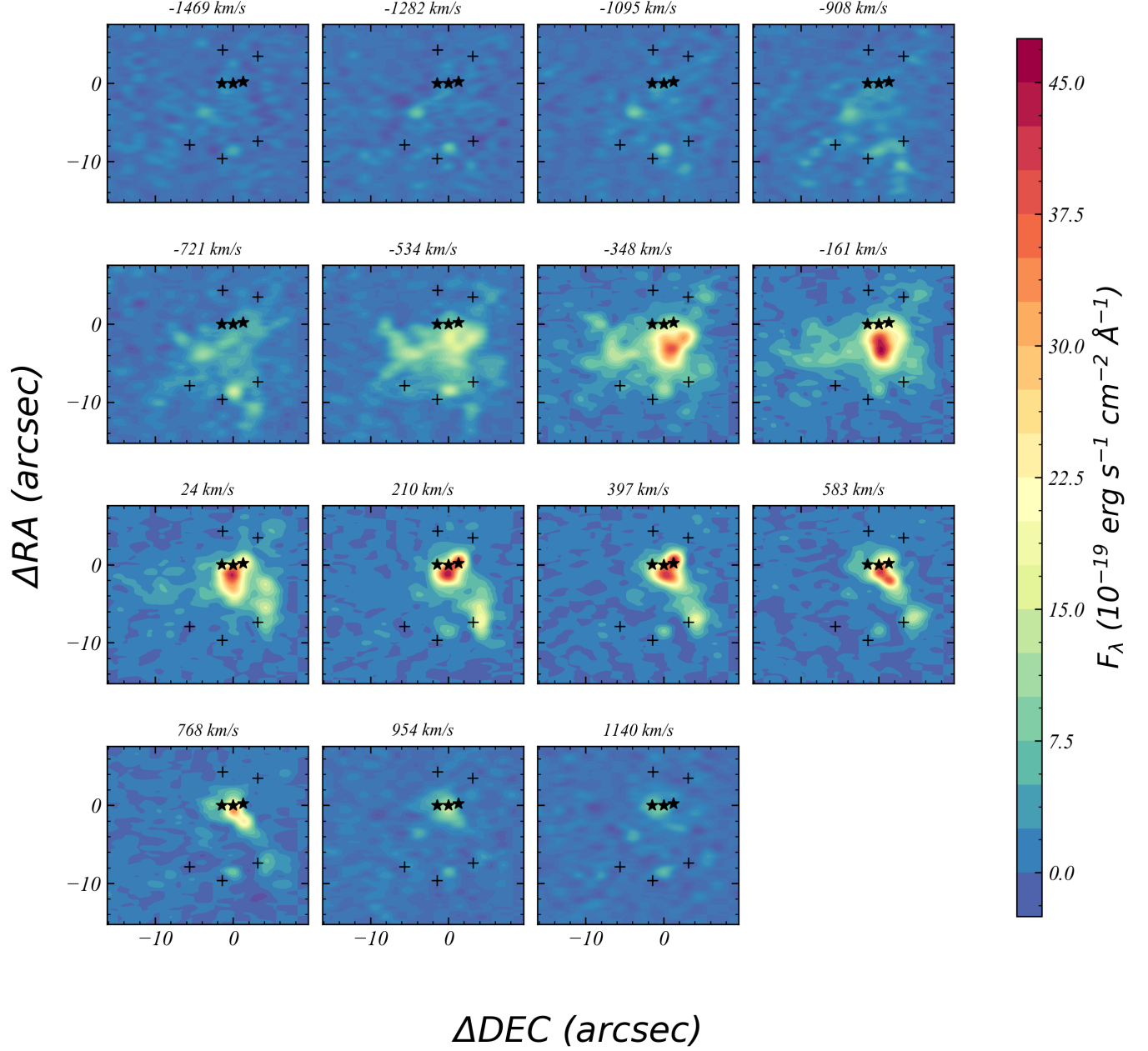


**Figure 5:** Channel maps for  $\text{Ly}\alpha$  emission in the wavelength coverage of 4000-4040 Å. We adopt  $\Delta v = 187$  km/s which corresponds to  $4 \text{ Å}^{-1}$  as the bin size. It shows fully separated red and blue components on either side of source-B which are the evidences of outflow.

Number	1	4	5	7	8	9	10	11	12	13	14	15	16	17	18	19	20	24	25
Velocity(km/s)	-416	-785	-649	-419	-515	-453	208	-157	-257	-424	-211	9	-75	-300	49	236	-267	182	-208
Dispersion(km/s)	618	342	392	626	319	474	450	174	219	444	269	415	799	242	668	481	358	660	472
$f_{\text{norm}}$	0.69	0.63	0.73	0.70	0.79	0.83	0.71	0.84	0.95	0.85	0.91	0.83	0.41	0.86	0.66	0.93	0.81	0.66	0.77



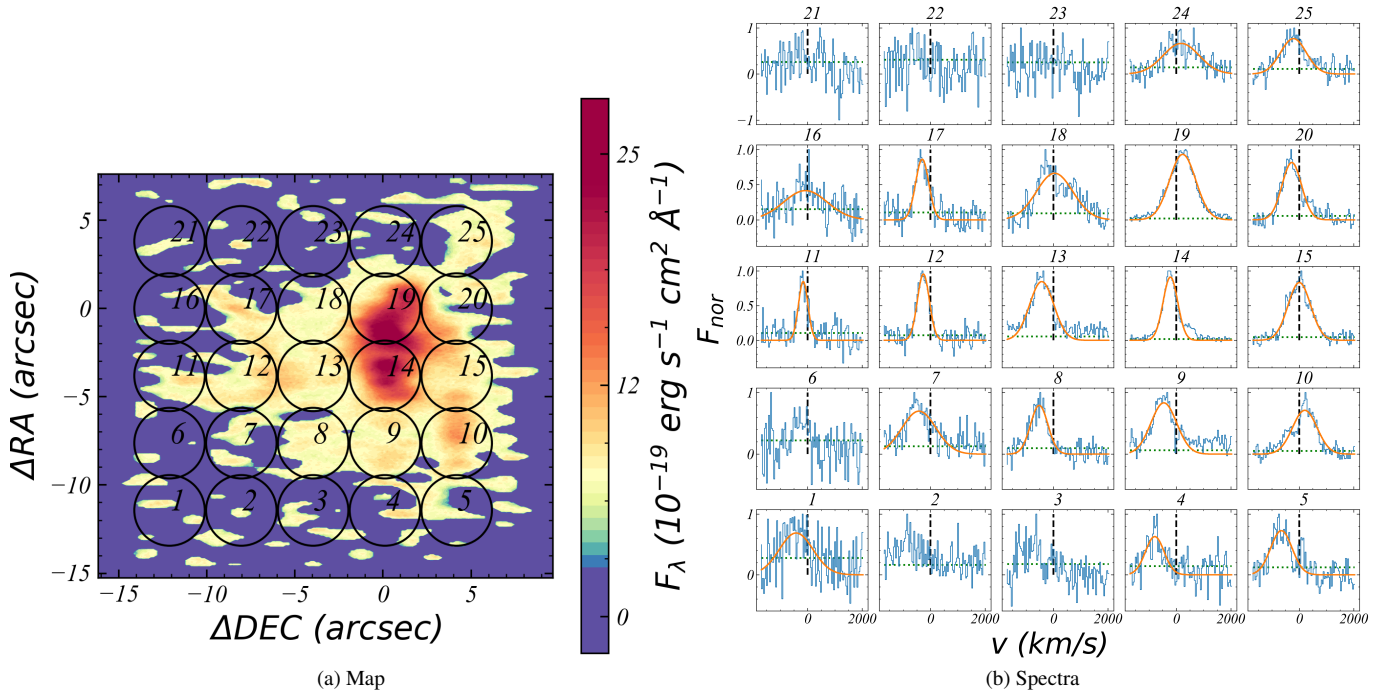


**Figure 6:** Left: Optimally extracted image of Ly $\alpha$  emission. The circular apertures and numbers indicate the spatial regions from which we extracted the spectra shown in the right panel. Right: continuum-subtracted spectra extracted from the individual spatial regions indicated in the left panel. The gray vertical lines represent the location of  $v = 0$  km/s, the green lines represent the noise level for each spectrum and the orange lines represent the fitting results of the Ly $\alpha$  emission for different spatial positions. The flux has been normalized.

line ratio SII  $\lambda 6716/\lambda 6731$ . Because this doublet is not covered by our IFU observations, we adopt the value  $n_e = 1.25 \text{ cm}^{-3}$  from Cai et al. (2017b). With the above equations and values, we obtain  $\dot{M}_{\text{out,low}} \approx 500 M_{\odot} \text{ yr}^{-1}$ . With the velocity dispersion  $\sigma_v = 600 \text{ km/s}$ , we derive the energy outflow rate to be  $\dot{E}_{\text{out,low}} \approx 10^{44} \text{ erg/s}$ .

To estimate the upper limit, we calculate the mass energy injection rates by assuming an energy conserving bubble in a uniform medium (Heckman et al. 1990) which gives the relation:

$$\dot{E}_{\text{out,up}} \approx 1.5 \times 10^{46} r_{10}^2 v_{1000}^3 n_{0.5} \text{ erg/s} \quad (4)$$

where  $r_{10}$  is the radius in unit of 10 kpc,  $v_{1000}$  in unit of 1000 km/s and  $n_{0.5}$  is in unit of  $0.5 \text{ cm}^{-3}$ . Using this method we obtain  $E_{\text{out,up}} \approx 9 \times 10^{46} \text{ erg/s}$ . The mass outflow rate is then given by  $\dot{M}_{\text{out,up}} = 2\dot{E}_{\text{out,up}}/c^2$  where  $c$  is the speed of light, this gives  $\dot{M}_{\text{out,up}} \approx 8.7 \times 10^5 M_{\odot} \text{ yr}^{-1}$ . So the fiducial value is  $\dot{E}_{\text{out,mean}} = 3 \times 10^{45} \text{ erg/s}$ .

In preparation for the follow discussion, we also estimate outflow momentum rate by taking the mass outflow rate calculated above and assuming  $\dot{P}_{\text{out}} = \dot{M}_{\text{out}} v_{\text{out}}$ .

## 4. Discussion

### 4.1. Outflow Driven Mechanism

In this section we will investigate which of these processes could be responsible for driving the extreme outflows observed. The dominant processes that drive such large scale

outflow in protocluster and the efficiency to which they are able to couple the gas are currently sources of uncertainty in galaxy formation models. Several possible mechanisms have been suggested to drive galaxy-wide outflows, for example: the stellar wind and supernovae; radiation pressure from the extremely luminous AGN or star formation; the interaction of radio jets with a clumpy and multiphase interstellar medium; AGN wind initially launched from the accretion disc. Following Harrison et al. (2014), we calculate the coupling efficiency which is a popular method to investigate the likely drivers of large-scale outflow. We compare the ratio of our outflow kinetic energy rate ( $E_{\text{out}}$ ) with (1) the AGN bolometric luminosity converted from AGN IR luminosity; (2) the star formation luminosity (Arrighi Battaia et al. 2018a). We also calculate the momentum-loading factor for both star-forming-driven case and AGN-driven case. Using these results we now explore the possible driving mechanisms to power this outflow.

Fig.?? shows coupling efficiency for both star-forming-driven case and AGN-driven case. We compare our result with results in Harrison et al. (2014). One way for star formation to drive large-scale outflow is by stellar winds or supernovae. An estimation of the coupling efficiency for this case is carried by Kennicutt Jr (1998), he found that the maximum coupling efficiency is  $E_{\text{out}}/L_{\text{IR,SF}} \approx 0.02$ , we indicate this upper limit with gray dot line in Fig.?. Based on this result, stellar winds and supernovae are unlikely to be fully

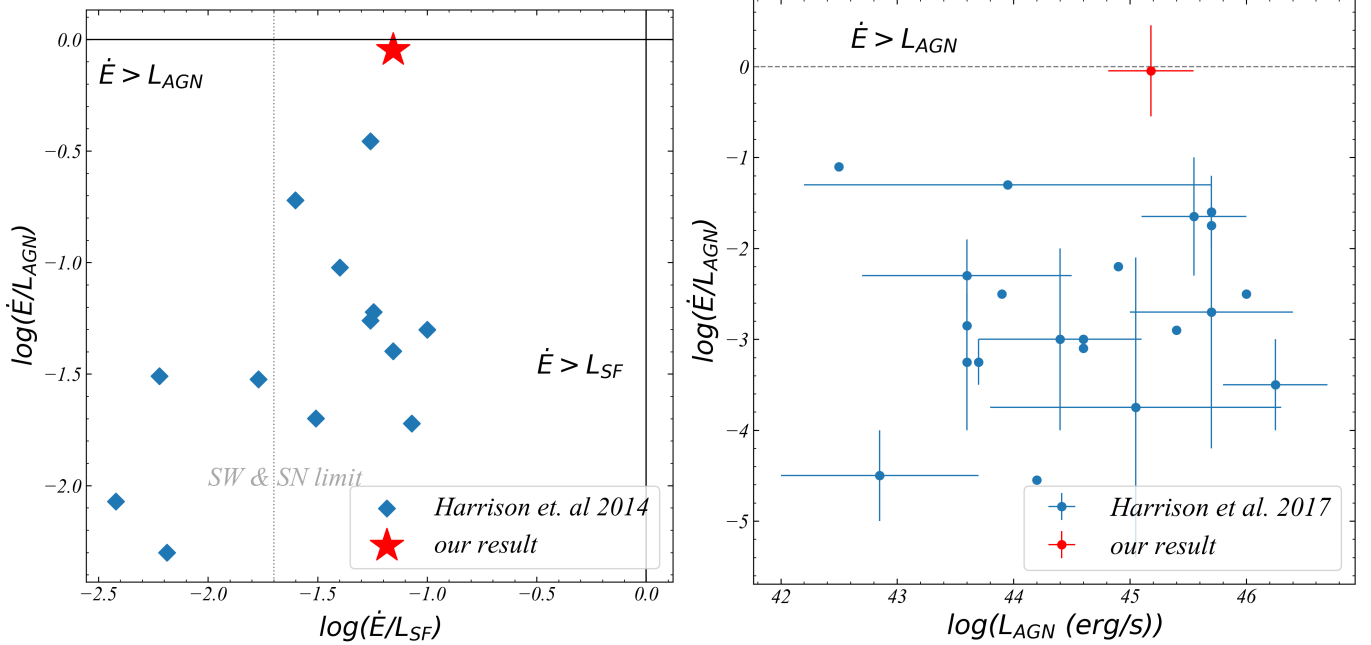


**Figure 7:** Left: the ratio of our estimated outflow kinetic energy rates ( $E_{\text{out}}$ ) to the AGN luminosity and to the star formation luminosity for our source (red) and sources from Harrison et al. (2014). The dashed vertical line is the estimated maximum mechanical input expected from supernovae and stellar winds. The two solid lines show the coupling efficiency of 1. Right: Observationally determined kinetic coupling efficiencies in Harrison et al. (2018) and our result. The vertical lines show the range of values quoted or, in the case of an error bar, the quoted error on the average value. The horizontal lines show the range of bolometric luminosity for each sample. The dotted line shows coupling efficiency of 1.

responsible to power outflow on physical scale of 100 kpc. By adopting a potential model for a halo with stellar mass  $M_* = 3 \times 10^{11} M_\odot$  at  $z \approx 2$  we run stellar feedback simulation, it shows the initial outflow velocity should reach 2300 km/s to meet our observation. However, neither of Heckman & Borthakur (2016) nor Li & Bryan (2020) shows stellar feedback can power such larger initial velocity which also indicates stellar formation is not a good interpretation for our case. On the other hand, the coupling efficiency for AGN-driven case is too large which is close to 1. In the right panel of Fig. ?? it shows that if the outflow is driven by AGN, it has already exceed other results with similar AGN luminosity.

Besides, if we instead consider a momentum-driven wind with momentum deposition from the radiation pressure of stars or AGN, the momentum loading factors are  $f_{\text{p,SF}} = 1.7$  and  $f_{\text{p,AGN}} = 3.2$  for the two mechanisms. Nevertheless Zubovas (2018) suggests that a typical momentum loading factor for star-formation-driven case is  $f_{\text{p,SF}} < 1.4$  which is lower than our estimation, this comparison also rules out the star-formation case. In the same way, we also find that  $f_{\text{p,AGN}}$  is larger than the typical value.

Moreover, Shankar et al. (2006) mentions the two sources of feedback have different effects over different mass ranges, in particular, stellar feedback regulates the processes in low-mass galaxies while large galaxies are mainly regulated by AGN feedback. The transition mass for this two feedback mechanisms is  $M_{\text{tr}} \approx 2 \times 10^{10} M_\odot$ . By fitting the SED of source-B, Arrigoni Battaia et al. (2018b) estimates its stellar

mass of source-B to be  $\log(M_{\text{star}}/M_\odot) = 11.4^{+0.3}_{-0.2}$ . Comparing with  $M_{\text{tr}}$ , it also confirms star-forming driven feedback is not the possible mechanism to power this outflow.

However, Zubovas (2018) also suggests there are mechanisms to reach high coupling efficiency and momentum loading factor. One possibility is hyper-Eddington Super Massive Black Hole (SMBH) growth during Compton-thick (heavily obscured) phase. In this case, SMBH would accrete material with extremely large rate and may lead to ultra fast outflows (UFO). Tombesi et al. (2013) shows the initial velocity is able to reach to  $0.1c$  and will have a strong coupling with the interstellar medium (ISM). Fig. 6 of Tombesi et al. (2013) shows the coupling efficiencies approximate 1 for some cases, but he also explains that this extremely fast and powerful outflow would occur only very close to SMBH  $R \approx 1000 r_s$  (where  $r_s$  is the schwarzschild radius.). He indicates that the large coupling efficiency is probably due to large environment column density  $\approx 10^{24} \text{ cm}^{-2}$  and highly ionized state which is similar to the large-scale environmental conditions of MAMMOTH-1. Cai et al. (2017b) suggests that the hydrogen column density is in the range  $10^{20} \text{ cm}^{-2}$ , with the presence of highly-coupling outflow we indicate here that the column density in CGM maybe  $10^3 \text{ cm}^{-2}$  larger than this value.

In summary, based on above analyses we find MAMMOTH-1 outflow is likely to be powered by AGN wind during the hyper-Eddington accretion of SMBH instead of star-forming processes. Although there is large uncertainty in the esti-

mation of coupling efficiency, the very-large-scale-effecting feedback is never observed before. If it is true, our result should be the first observation of AGN-mode feedback on 100 kpc. It puts a very strong constrain on galaxies feedback processes and even further affects our understanding of galaxy evolution.

#### 4.2. Galaxy Group Systems

Cai et al. (2017a) demonstrates MAMMOTH-1 is in the density peak of BOSS1441 protocluster with overdensity  $\sigma = 10.8 \pm 2.6$ . Arrigoni Battaia et al. (2018a) finds the observed flux of BOSS1441 have good agreement with SED template of M82 which is a starburst galaxy. He estimates its far-infrared luminosity (rest-frame  $8 - 1000\mu\text{m}$ )  $L_{\text{FIR}} = 3.2_{-2.1}^{+7.4} \times L_{\odot}$  which meets the criteria used to define ultra luminous infrared galaxy (ULIRG). Beside, the star-formation rate is also obtained by  $\text{SFR} = 400 M_{\odot} \text{ yr}^{-1}$ . Based on the large SFR and the mass outflow rate  $\dot{M}_{\text{out}} \approx 500 M_{\odot} \text{ yr}^{-1}$ , we note that there should be a lot of gas injecting into the central AGN to supply the gas consumption. Furthermore, eight sources have been spectroscopically confirmed at  $z = 2.32$  by our submillimeter observations (Li et al. 2020) with our HST imaging even revealing three sources within  $3''$ . All of these evidences indicate that this is highly likely to be an violently interacting galaxy system.

We suggest that the physical picture of this area is like this: the three central sources are wildly interacting with each others. The middle source continues to accrete material from others to supply its SMBH growth, star formation and meanwhile producing strong outflow. Owing to the tidal effect between the three sources, a lot of material is pulled out from galaxies and densifies the gas environment which consequently lead to the quasar heavily obscured. This dense gas environment can also naturally explain why there is strong coupling between outflow and environment.

#### 4.3. Nebula powering mechanism

Cantalupo (2017) demonstrates there are three physical processes that are able to produce extended and bright  $\text{Ly}\alpha$  emission. The first is the recombination radiation following hydrogen photoionization, the second is  $\text{Ly}\alpha$  scattering of photons produced by a nearby star forming galaxy or quasar, and the last is  $\text{Ly}\alpha$  collisional excitation and recombination radiation also known as shock heating. Leibler et al. (2018) shows that the expected  $\frac{F_{\text{Ly}\alpha}}{F_{\text{H}\alpha}}$  ratio for the "case B" of photoionization recombination should range between 8.1-11.6. The mean ratio for "region 1" is 0.314 and 6.8 for "region 2". This shows  $\text{H}\alpha$  emission is much weaker than  $\text{Ly}\alpha$  emission in "region 1" which indicates "case B" of fluorescence is unlikely to be the dominant powering mechanism. In addition, due to the powerful outflow discovered in this nebula, this enormous  $\text{Ly}\alpha$  nebula is likely to be powered by the shock heating. Because source-B is a starburst quasar confirmed by the SED fitting, it should have strong UV emissions to power the fluorescence. Moreover, due to the decline of ratio from edge to center, we note that shock heating and fluorescence may both contribute to the  $\text{Ly}\alpha$  emission. Shock

heating dominant the emission in the central region while fluorescence may play a role in peripheral region.

### 5. Conclusions

In this paper, we present our follow-up observations on MAMMOTH-1 in the density peak of large-scale structure BOSS1441 at  $z = 2.31$  with the newly-onboard KCWI. With the powerful IFU observations, we are allowed to have a deep insight into this enormous  $\text{Ly}\alpha$  nebula. The main conclusion of this paper are as follows:

(1) With the optimally-extracted images, we find  $\text{Ly}\alpha$  extends to 175 kpc with the surface brightness of  $\text{SB}_{\text{Ly}\alpha} = 6.4 \times 10^{-18} \text{ erg s}^{-1} \text{ cm}^{-2} \text{ arcsec}^{-2}$ . Besides, we reveal  $\text{HeII}$  and  $\text{CIV}$  emission on 80 kpc and 88 kpc with the surface brightness of  $\text{SB}_{\text{HeII}} = 9.2 \times 10^{-19} \text{ erg s}^{-1} \text{ cm}^{-2} \text{ arcsec}^{-2}$  and  $\text{SB}_{\text{CIV}} = 3.8 \times 10^{-18} \text{ erg s}^{-1} \text{ cm}^{-2} \text{ arcsec}^{-2}$  respectively. Furthermore, the NB image obtained with MOIRCS on Subaru Telescope also reveals  $\text{H}\alpha$  emission on 122 kpc. The ratio map obtained from  $\text{H}\alpha$  and  $\text{Ly}\alpha$  emission indicates the "case B" of fluorescence and shock-heating both contribute to the  $\text{Ly}\alpha$  emission. With the ratio decreasing from edge to center, we note the "case B" of fluorescence should power the emissions in marginal region while shock-heating play an important role in the inner region. The rarely seen very extended  $\text{H}\alpha$  emission makes this system even more unique.

(2) The velocity gradients revealed from the three-dimensional kinematics of  $\text{Ly}\alpha$ ,  $\text{HeII}$  and  $\text{CIV}$  emissions have the same direction with velocity offset of  $\Delta v = 1000 \text{ km/s}$ . In addition, the dispersion map of  $\text{Ly}\alpha$  emission shows an extended region centering on source-B possesses larger velocity dispersion ( $\sigma_v > 400 \text{ km/s}$ ) than the expectation in dark matter halo. In some spatial position, the dispersion even reach to 650 km/s which corresponds to 1550 km/s for FWHM. With the presence of extended metal lines and the unique kinematics, outflow from source-B is the most natural explanation.

(3) To find the possible mechanisms powering this outflow, we firstly fit the observed flux of source-B with M82 SED and compare it with the SED or radio fluxes of galaxies with significant radio emission. This comparison confirms that source-B should be a radio-quiet quasar, so radio jet is not the powering mechanism. We further estimate the energy outflow rate  $\dot{E}_{\text{out}} = 3 \times 10^{45} \text{ erg/s}$  and its coupling efficiency. Comparing these results with simulations, we find quasar-mode feedback is the only mechanism which can power this outflow. The rare seen outflow powered by quasar-mode feedback on CGM scale makes our observations very unique and will further help us to understand its role in the coevolution of galaxies and their gas environments.

### References

Arrigoni Battaia, F. et al. 2018a, *Astronomy & astrophysics.*, 620, A202

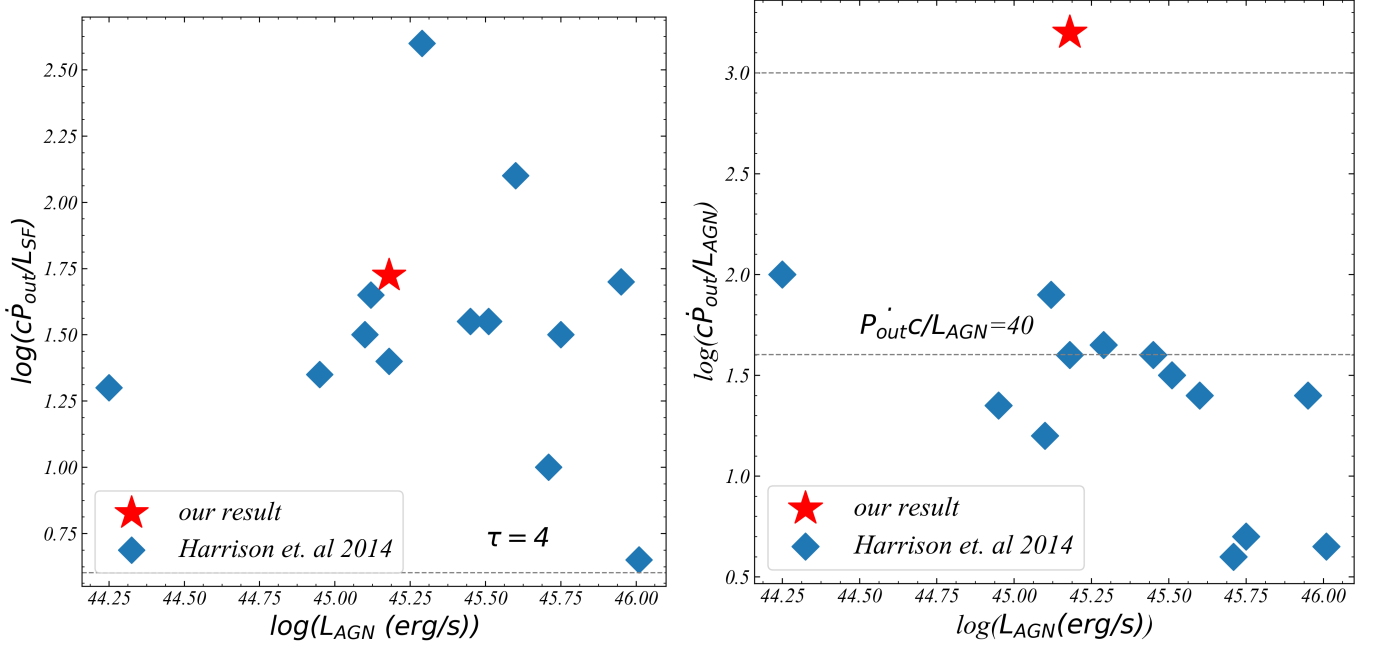


**Figure 8:** Left: momentum rates of the outflows ( $\dot{P}_{out}$  normalized to the star formation luminosity  $L_{SF}/c$  versus AGN luminosity. The dashed lines represent the required optical depths if the outflows are driven by radiation pressure from star formation. Right: momentum rate of outflows normalized to AGN luminosity ( $L_{AGN}/c$ ) versus AGN luminosity. Based on our assumptions, the outflows are unlikely to be purely radiatively driven, the ratio is also too high for theoretical predictions of energy-driven outflows launched by AGN accretion-disc wind.

Arrigoni Battaia, F., Hennawi, J. F., Prochaska, J. X., Oñorbe, J., Farina, E. P., Cantalupo, S., & Lusso, E. 2018b, *Monthly Notices of the Royal Astronomical Society*, 482, 3162

Arrigoni Battaia, F., Hennawi, J. F., Prochaska, J. X., Oñorbe, J., Farina, E. P., Cantalupo, S., & Lusso, E. 2018, *Monthly Notices of the Royal Astronomical Society*, 482, 3162–3205

Benson, A., Bower, R., Frenk, C., Lacey, C. G., Baugh, C., & Cole, S. 2003, *The Astrophysical Journal*, 599, 38

Booth, C. M., & Schaye, J. 2009, *Monthly Notices of the Royal Astronomical Society*, 398, 53–74

Borgani, S., Fabjan, D., Tornatore, L., Schindler, S., Dolag, K., & Diaferio, A. 2008, *Space Science Reviews*, 134, 379

Borisova, E. et al. 2016, *The Astrophysical Journal*, 831, 39

Bower, R. G., Benson, A., Malbon, R., Helly, J., Frenk, C., Baugh, C., Cole, S., & Lacey, C. G. 2006, *Monthly Notices of the Royal Astronomical Society*, 370, 645

Cai, Z. et al. 2017a, *The Astrophysical Journal*, 839, 131

Cai, Z. et al. 2017b, *The Astrophysical Journal*, 837, 71

Cantalupo, S. 2017, *Astrophysics and Space Science Library*, 195–220

Cantalupo, S., Porciani, C., Lilly, S. J., & Miniati, F. 2005, *Astrophysical Journal*, 628, págs. 61

Churazov, E., Sazonov, S., Sunyaev, R., Forman, W., Jones, C., & Böhringer, H. 2005, *Monthly Notices of the Royal Astronomical Society: Letters*, 363, L91

Ciotti, L., & Ostriker, J. P. 2007, *The Astrophysical Journal*, 665, 1038–1056

Ciotti, L., Ostriker, J. P., & Proga, D. 2010, *The Astrophysical Journal*, 717, 708

Ciotti, L., Pellegrini, S., Negri, A., & Ostriker, J. P. 2017, *The Astrophysical Journal*, 835, 15

Croton, D. J. et al. 2006, *Monthly Notices of the Royal Astronomical Society*, 365, 11

DeBuhr, J., Quataert, E., & Ma, C.-P. 2012, *Monthly Notices of the Royal Astronomical Society*, 420, 2221

Del Moro, A. et al. 2013, *Astronomy & Astrophysics*, 549, A59

Di Matteo, T., Springel, V., & Hernquist, L. 2005, *Nature*, 433, 604–607

Emonts, B. H., Cai, Z., Prochaska, J. X., Li, Q., & Lehnert, M. D. 2019, *The Astrophysical Journal*, 887, 86

Fabian, A. 1999, *Monthly Notices of the Royal Astronomical Society*, 308, L39

Fabian, A. 2012, *Observational evidence of AGN feedback*

Fabjan, D., Borgani, S., Tornatore, L., Saro, A., Murante, G., & Dolag, K. 2010, *Monthly Notices of the Royal Astronomical Society*, 401, 1670

Faucher-Giguère, C.-A., & Quataert, E. 2012, *Monthly Notices of the Royal Astronomical Society*, 425, 605

Faucher-Giguère, C.-A., Feldmann, R., Quataert, E., Kereš, D., Hopkins, P. F., & Murray, N. 2016, *Monthly Notices of the Royal Astronomical Society: Letters*, 461, L32–L36

Granato, G. L., De Zotti, G., Silva, L., Bressan, A., & Danese, L. 2004, *The Astrophysical Journal*, 600, 580

Harrison, C., Alexander, D., Mullaney, J., & Swinbank, A. 2014, *Monthly Notices of the Royal Astronomical Society*, 441, 3306

Harrison, C., Costa, T., Tadhunter, C., Flötsch, A., Kakkad, D., Perna, M., & Vietri, G. 2018, *Nature Astronomy*, 2, 198

Harrison, C. M. 2016, *Observational constraints on the influence of active galactic nuclei on the evolution of galaxies* (Springer)

Heckman, T. M., Armus, L., Miley, G. K., et al. 1990, *Astrophysical Journal Supplement Series*, 74, 833

Heckman, T. M., & Borthakur, S. 2016, *Astrophysical Journal*, 822, 9

Hennawi, J. F., & Prochaska, J. X. 2013, *The Astrophysical Journal*, 766, 58

Hirschmann, M., Dolag, K., Saro, A., Bachmann, L., Borgani, S., & Burkert, A. 2014, *Monthly Notices of the Royal Astronomical Society*, 442, 2304–2324

Hopkins, A. M., & Beacom, J. F. 2006, *The Astrophysical Journal*, 651, 142



- Ishibashi, W., & Fabian, A. 2012, *Monthly Notices of the Royal Astronomical Society*, 427, 2998
- Ivison, R. et al. 2010, *Astronomy & Astrophysics*, 518, L31
- Kennicutt Jr, R. C. 1998, *Annual Review of Astronomy and Astrophysics*, 36, 189
- King, A., Zubovas, K., & Power, C. 2011, *Monthly Notices of the Royal Astronomical Society: Letters*, 415, L6
- Lau, M. W., Prochaska, J. X., & Hennawi, J. F. 2016, *The Astrophysical Journal Supplement Series*, 226, 25
- Leibler, C. N., Cantalupo, S., Holden, B. P., & Madau, P. 2018, *Monthly Notices of the Royal Astronomical Society*, 480, 2094–2108
- Li, M., & Bryan, G. L. 2020, *The Astrophysical Journal*, 890, L30
- Li, Q., aa, c., & bb, d. 2020, in prep
- McCarthy, I. G., Schaye, J., Bower, R. G., Ponman, T. J., Booth, C. M., Vecchia, C. D., & Springel, V. 2011, *Monthly Notices of the Royal Astronomical Society*, 412, 1965
- Nayakshin, S., & Zubovas, K. 2012, *Monthly Notices of the Royal Astronomical Society*, 427, 372
- Nesvadba, N., Lehnert, M., De Breuck, C., Gilbert, A., & Van Breugel, W. 2008, *Astronomy & Astrophysics*, 491, 407
- Nesvadba, N. P. H., Lehnert, M. D., Eisenhauer, F., Gilbert, A., Tecza, M., & Abuter, R. 2006, *The Astrophysical Journal*, 650, 693–705
- Ostriker, J. P., Choi, E., Ciotti, L., Novak, G. S., & Proga, D. 2010, *The Astrophysical Journal*, 722, 642–652
- Prochaska, J. X. et al. 2013, *The Astrophysical Journal*, 776, 136
- Rodriguez Zaurin, J., Tadhunter, C., Rose, M., & Holt, J. 2013, *Monthly Notices of the Royal Astronomical Society*, 432, 138
- Rupke, D. S. et al. 2019, *Nature*, 574, 643
- Shankar, F., Lapi, A., Salucci, P., De Zotti, G., & Danese, L. 2006, *The Astrophysical Journal*, 643, 14
- Sijacki, D., Springel, V., Di Matteo, T., & Hernquist, L. 2007, *Monthly Notices of the Royal Astronomical Society*, 380, 877–900
- Silk, J. 2013, *The Astrophysical Journal*, 772, 112
- Silva, L., Granato, G. L., Bressan, A., & Danese, L. 1998, *The Astrophysical Journal*, 509, 103
- Somerville, R. S., Hopkins, P. F., Cox, T. J., Robertson, B. E., & Hernquist, L. 2008, *Monthly Notices of the Royal Astronomical Society*, 391, 481
- Springel, V., Di Matteo, T., & Hernquist, L. 2005, *Monthly Notices of the Royal Astronomical Society*, 361, 776–794
- Storey, P., & Hummer, D. 1995, *Monthly Notices of the Royal Astronomical Society*, 272, 41
- Toba, Y. et al. 2019, *The Astrophysical Journal Supplement Series*, 243, 15
- Tombesi, F., Cappi, M., Reeves, J., Nemmen, R., Braitto, V., Gaspari, M., & Reynolds, C. 2013, *Monthly Notices of the Royal Astronomical Society*, 430, 1102
- Wiersma, R. P., Schaye, J., Theuns, T., Dalla Vecchia, C., & Tornatore, L. 2009, *Monthly Notices of the Royal Astronomical Society*, 399, 574
- Zubovas, K. 2018, *Monthly Notices of the Royal Astronomical Society*, 479, 3189